INTERNATIONAL JOURNAL OF CONTROL
2021, VOL. 94, NO. 4, 1102–1113
https://doi.org/10.1080/00207179.2019.1632491

Taylor & Francis
Taylor & Francis Group

Energy maximising robust control for spectral and pseudospectral methods with application to wave energy systems

Demián Garcia-Violini and John V. Ringwood

Centre for Ocean Energy Research, Maynooth University, Ireland

ABSTRACT

Spectral and *Pseudospectral* methods have been widely considered in diverse optimal control applications, usually where energy optimisation is required. Although such methods are a good way to ensure a good balance between performance and computational effort, in most of the literature, nominal mathematical models are considered without taking into account possible dynamic deviations from the nominal case. The main aim of this study is to propose a novel framework where spectral and pseudospectral problems include some structured uncertainty, achieving robust optimal control designs guaranteeing the 'best worst-case performance'. In this paper, the objective function used for optimisation is inspired by wave energy converters. Two solution methodologies are developed. Firstly, an analytical solution, for circular and convex polytopic uncertainty boundaries, is proposed. Then, a numerical formulation is introduced to consider uncertainty sets of arbitrary shape, adding the ability to consider physical system constraints. Finally, an application example shows the benefit of this new control formulation.

ARTICLE HISTORY
Received 7 September 2018
Accepted 8 June 2019

KEYWORDS
Control; robust; spectral; pseudospectral; optimisation; energy maximising

1. Introduction

Spectral and pseudospectral methods, both members of the family of *Direct Transcription Methods*, have been widely reported in the bibliography in diverse optimal control applications, such as boundary value and eigenvalue problems, and also objective function optimisation (maximisation or minimisation). These methods discretise the problem and find approximate solutions where the accuracy and performance can be progressively improved by increasing the number of basis functions (Genest & Ringwood, 2017). In addition, one reason for the popularity of these methods is the user-selectable trade-off between computational effort and solution precision. However, to date, robust approaches, which allow for the description of the system with dynamical uncertainty, are not available (Faedo, Olaya, & Ringwood, 2017). On the other hand, indirect methods, which seek the optimal solution using analytical tools, are problem-dependent, since they need a precise analytical description. Furthermore, the region of convergence for the optimal solution is typically small (Bacelli & Ringwood, 2015).

Spectral and pseudospectral methods are based on the employment of the Mean-Weighted Residual (MWR) technique. The particular definition of the finite-dimensional orthogonal set of test (or weight) functions ψ_i, used to solve for the annulment of the so-called *residual* function, distinguishes spectral from pseudospectral methods. If the set of test functions ψ_i are elements of the same set as the basis functions ϕ_i which approximate the state vector of the system, then the method is known as a *spectral* or *Galerkin* method. On the other hand, if the test functions are translated Dirac-Deltas $\delta(t - t_i)$, the method takes the name of a *pseudospectral*, *collocation*, or *interpolation* method. However, common to both approaches is the projection of the residual function onto the set of test functions and, regardless of the basis functions selected, is cancelled. A complete discussion of MWR techniques can be found in (Finlayson & Scriven, 1966). Numerical optimal control, utilising spectral and pseudospectral methods, is treated in depth by Fornberg (1996), Boyd (2001), and Bacelli (2014). In Bacelli, Ringwood, and Gilloteaux (2011) and Herber and Allison (2013), application examples of spectral and pseudospectral methods, respectively, applied to the wave energy application, can be found. The reader is referred to Gong, Kang, and Ross (2006), Fahroo and Ross (2008), Ross and Karpenko (2012), Liu and Li (2014), and Nikooeinejad, Delavarkhalafi, and Heydari (2018) for further general control applications employing spectral and pseudospectral methods.

For the growing area of Wave Energy Converter (WEC) maximising control (Ringwood, Bacelli, & Fusco, 2014), spectral and pseudospectral methods have been demonstrated to be appealing. The features which make spectral and/or pseudospectral methods useful in that application are worth highlighting. Firstly, the oscillatory nature that governs the problem makes this approach interesting, since waves can be approximately described as a multi-periodic process. With the purpose of approximating the periodic nature of the problem, the use of spectral and pseudospectral methods, with *Fourier* and *Chebyshev-Fourier* basis functions, has been shown by Bacelli and Ringwood (2015) and Genest and Ringwood (2017), respectively. On the other hand, the use of these methods in WEC control also has a significant impact on the simplification of a convolution integral associated with the radiation force.

CONTACT Demián Garcia-Violini demian.garciaviolini@mu.ie

In particular, as shown in Bacelli and Ringwood (2015), the numerical computation of the convolution integral can be carried out off-line, thus significantly reducing the computational load when solving the nonlinear program. The final aspect that makes the WEC control problem amenable, using MWR-based methods, is the transformation of the integral objective function that should be maximised. As will be shown later, the integral objective function is significantly simplified by converting it into an algebraic equation.

Although MWR-based methods have been widely used to address different applications with linear and nonlinear descriptions, most of the recent literature uses these methods in a non-robust sense, without considering possible dynamic deviation (uncertainties) from the nominal model (Faedo et al., 2017). While adaptive control is a way to deal with possible uncertainties, adaptive approaches do not give guarantees of convergence as shown by Davidson, Genest, and Ringwood (2018). Furthermore, while nonlinear approaches can deal with nonlinear deviation from a linear model, these approaches depend on a precise description of the nonlinear model and are often limited to specific aspects of control, which falls within the traditional category of regulatory/servo feedback control, for which robust methodologies are available. Examples of the synthesis of robust WEC controllers can be found in, for example, Fusco and Ringwood (2014) and Wahyudie, Jama, and Saed (2015).

Considering the lack of robustness analysis for spectral and pseudospectral methods in general control problems, and particularly for energy maximising performance objectives, this paper redefines the spectral/pseudospectral control problem, taking dynamical uncertainty into account. The objective of the proposed framework is to ensure the 'Best Worst-Case Performance' (Best-WCP).[1] This involves the determination of a control signal which minimises the performance degradation in the objective function, when the system under study has uncertainty in its description. Then, a procedure to solve this new optimal problem is proposed, as well as a means to compute its solution. Two methodologies are developed. Firstly, an analytical and explicit solution for circular and convex polytopic uncertainty boundaries is proposed. Then, the scope of the problem is extended via a numerical formulation to consider uncertainty sets of arbitrary shape, also adding the ability to consider physical system constraints.

The remainder of this paper is organised as follows. The basics of spectral and pseudospectral control, and the derivation of the objective function are recalled in Section 2. Section 3 develops and solves the optimisation problem which will guarantee the Best-WCP condition. Section 4, using data for a spherical WEC model, demonstrates an application example which illustrates the benefit of this new control formulation in cases where modelling errors typically arise. Finally, conclusions on the overall application of the proposed method are provided in Section 5.

2. Control problem preliminaries

The purpose of this section is to state the basic ideas that will be used in the development of the robust method in Section 3. With this aim, this section is divided into three stages. In Section 2.1, general concepts around spectral and pseudospectral methods, are recalled. The objective function is introduced and approximated by the use of the methods presented in Section 2.1. Finally, in Section 2.3, the optimal control results for the nominal case are shown. This section can be studied in-depth following the development performed in Fornberg (1996) or Bacelli and Ringwood (2015).

2.1 Spectral and pseudospectral methods

Spectral and pseudospectral methods are based on an approximation of the states and control variables into an n-dimensional vector space spanned by an orthogonal basis of real functions $\Phi = \{\phi_i\}_{i=1}^{N}$. The system's states and control are commonly approximated as:

$$x_i(t) \approx x_i^N(t) = \sum_{j=1}^{N} \phi_j(t) x_{ij} = \Phi(t)\hat{\mathbf{x}}_i \tag{1a}$$

$$u(t) \approx u^N(t) = \sum_{j=1}^{N} \phi_j(t) u_j = \Phi(t)\hat{\mathbf{u}} \tag{1b}$$

with $\Phi(t) = [\phi_1(t) \ \dots \ \phi_N(t)]$, an orthogonal set of basis functions, $\hat{\mathbf{x}}_i = [x_{i1} \ \dots \ x_{iN}]^\intercal \in \mathbb{R}^N$, and $\hat{\mathbf{u}} = [u_1 \ \dots \ u_N]^\intercal \in \mathbb{R}^N$. The sets of coefficients $\{x_{ij}\}$ and $\{u_j\}$ are determined by forcing the projection of the residual functions over the set of test functions $\Psi = \{\psi_j\}_{j=1}^{N}$ to be zero. When $\psi_j = \delta(t - t_j)$, i.e. translated Dirac-Delta functions, then the method is called pseudospectral, and guarantees the interpolation at t_j. When the set of test functions is defined by a truncated generalised Fourier series and $\{\phi_j\} = \{\psi_j\} \forall j = 1, \dots, N$, the method is known as spectral. In general, MWR-based methods can use a wide variety of test functions, depending on the suitability for particular applications.

2.2 Objective function

As mentioned in Section 1, the objective function used in WEC control has features that make it amenable to spectral or pseudospectral methods. In order to introduce the objective function used in this study, the WEC control basics are recalled in the following. Note that the WEC modelling assumptions considered in this section are consistent across a wide variety of WEC energy-maximising model-based optimal control applications presented in the literature, such as, for example, Richter, Magaña, Sawodny, and Brekken (2014), Li and Belmont (2014), Bacelli and Ringwood (2015), and Genest and Ringwood (2016).

Considering that the WEC device is referenced from its equilibrium position (still water level) in an undisturbed wave field and immersed in an infinite-depth sea, the system is subject to fluid-structure interactions which are typically modelled using potential flow theory. The fluid is assumed to be inviscid and incompressible, and the flow is considered irrotational. By applying Newton's second law to the WEC device, the following linear hydrodynamic formulation is obtained:

$$M\ddot{x}_p(t) = F_b(t) + F_r(t) + F_e(t) + u(t), \tag{2}$$

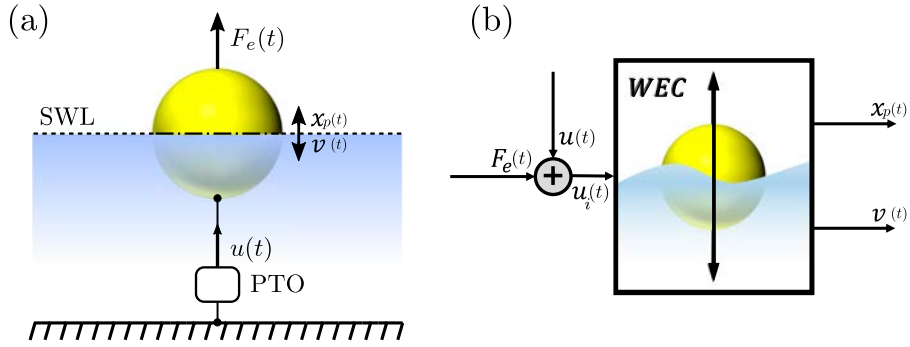

Figure 1. (a) A single-body floating system, oscillating in heave, is schematically depicted. The lower side of the power take-off is anchored to the sea bed, which provides an absolute reference for device motion. Still water level is denoted by the acronym SWL. (b) Scheme of a general WEC device. $F_e(t)$ represents the excitation force and $u(t)$ represents the control input. The outputs are the WEC position and velocity, $x_p(t)$ and $v(t)$, respectively. The control objective is to capture the maximum possible energy.

where M is the mass of the WEC (system), $F_b(t)$ the hydrostatic restoring force, $F_r(t)$ the radiation force, $F_e(t)$ the wave excitation force, $u(t)$ the control force applied through the Power Take-Off (PTO) system, and $x_p(t)$, $\dot{x}_p(t) = v(t)$ and $\ddot{x}_p(t)$ are the WEC position, velocity, and acceleration, respectively. Both the excitation force and the control force are external forces acting on the system. A single-body floating system, oscillating in heave, is schematically depicted in Figure 1(a). The hydrostatic force for a floating body is written as $F_b(t) = \rho g(V_i - V_0)$, where ρ is the water density, g is the acceleration due to gravity, and $V_i = V_0 - S_h x_p(t)$ represents the immersed volume of the WEC, with V_0 the immersed volume at the equilibrium position and $-S_h x_p$ a linear approximation of the additional immersed volume, depending on the position of the system. The radiation force $F_r(t)$, which is modelled using linear potential theory, is

$$F_r(t) = -\int_0^{+\infty} h_r(\tau)\dot{x}_p(t-\tau)\,\mathrm{d}\tau - m_\infty \ddot{x}_p(t), \tag{3}$$

where $m_\infty > 0$ represents the added mass at infinite frequency and $h_r(t)$ is the (causal) radiation impulse response (Falnes, 2002). In general, $F_r(t)$, in Equation (3), is a damping/inertial force arising due to the fact that the device motion, resulting in the production of radiated waves, is affected by the surrounding fluid. Then, Equation (2) results in the linearised equation of motion known as Cummins' equation (Cummins, 1962)

$$(M + m_\infty)\ddot{x}_p(t) + \int_0^{+\infty} h_r(\tau)\dot{x}_p(t-\tau)\,\mathrm{d}\tau + s_h x_p(t) = F_e(t) + u(t), \tag{4}$$

where $s_h = \rho g S_h \geq 0$ corresponds to the hydrostatic stiffness. In addition, in Equation (4), the excitation force $F_e(t)$ is related to the incident surface elevation $\eta(t)$ through an excitation kernel function $h_{ex}(t)$, particular to each specific WEC device. Typically, $h_r(t)$ and $h_{ex}(t)$ are calculated numerically using boundary-element potential methods (Babarit & Delhommeau, 2015). Finally, the useful absorbed energy is extracted from the relative displacement with an absolute reference for device motion, usually the sea bottom, through the PTO system. The reader is referred to Falnes (2002) for an exhaustive description of WEC dynamics.

The useful absorbed energy over the time interval $[0\ T]$, $T > 0$, can be calculated as the integral of converted power, involving the control force $u(t)$, applied through the PTO system, and the velocity of the device $v(t)$:

$$J \equiv E = -\int_0^T P\,\mathrm{d}t = -\int_0^T v^\intercal(t)u(t)\,\mathrm{d}t. \tag{5}$$

where E represents the absorbed energy, P the instantaneous power, and $u(t)$ and $v(t)$, defined in Equation (2), are the control force and the WEC velocity, respectively, while the WEC device is moving under the influence of the forces depicted in Equation (4). Equation (5) defines the objective function J used both in general WEC maximising control problems and for this study. The method proposed in this study (Section 3) can be applied to more generic cases in which the objective function matches that presented in Equation (5). For example, in a general electrical renewable energy application, e.g. solar power maximisation, v(t) would be replaced by current, and u(t) by voltage, in Equation (5). Figure 1(b) shows a general WEC device where the objective is to capture the maximum possible energy. $F_e(t)$ represents the excitation force and $u(t)$ represents the control input. The outputs are the WEC position and velocity, $x_p(t)$ and $v(t)$, respectively.

Due to the orthogonality of the basis functions ϕ_j, the application of spectral or pseudospectral approximation to the objective function J, as in Equation (1), results in:

$$J \approx J_N = \int_0^T \hat{\mathbf{u}}^\intercal \Phi^\intercal(t)\Phi(t)\hat{\mathbf{v}} = -\frac{T}{2}\hat{\mathbf{u}}^\intercal\hat{\mathbf{v}}, \tag{6}$$

where $\hat{\mathbf{v}} = [v_1\ v_2\ \ldots\ v_N]^\intercal \in \mathbb{R}^N$ corresponds to the approximation of $v(t)$, which can be obtained by a linear combination of the approximate states $\hat{\mathbf{x}}_i$ defined in Equation (1a), and $\hat{\mathbf{u}} = [u_1\ u_2\ \ldots\ u_N]^\intercal$ is stated in Equation (1b). It can be easily seen how the integral relationship becomes an algebraic one, as shown in Equation (6).

Given the set Φ of basis functions, suppose that

$$\dot{\Phi}(t) = \Phi(t)\mathbf{D},$$

where $\mathbf{D} \in \mathbb{R}^{n\times n}$, holds. Then

$$\hat{\mathbf{v}} = \mathbf{G_o}(\hat{\mathbf{u}} + \hat{\mathbf{e}}), \tag{7}$$

where $\mathbf{G_o} \in \mathbb{R}^{N\times N}$, defined as the system *model*, represents the mapping between $\hat{\mathbf{u}} + \hat{\mathbf{e}}$, which is the approximation of the total input force $u_i(t) = u(t) + F_e(t)$, and $\hat{\mathbf{v}}$, which is the approximation of the output velocity $v(t)$. Furthermore, in Equation (7), $\hat{\mathbf{e}} = [e_1\ e_2\ \dots\ e_N]^\intercal \in \mathbb{R}^N$, where e_i, $i \in \{1,\dots,N\}$, represent the coefficients of the excitation force $F_e(t)$ approximation on the basis defined by $\Phi(t)$, i.e. $F_e(t) \approx \Phi(t)\hat{\mathbf{e}}$, as shown for the control signal $u(t)$ in Equation (1b). The basis functions are chosen such that $\mathbf{G_o}$ satisfies

$$\mathbf{G_o} = \bigoplus_{k=1}^{N/2} \begin{bmatrix} \mathcal{R}_k^o & \mathcal{I}_k^o \\ -\mathcal{I}_k^o & \mathcal{R}_k^o \end{bmatrix}, \tag{8}$$

with $\mathcal{R}_k^o, \mathcal{I}_k^o \in \mathbb{R}$, $\mathbf{G_o} \in \mathbb{R}^{N\times N}$ and the symbol $\bigoplus$ denotes the direct sum of n matrices, i.e. $\bigoplus_{i=1}^n A_i = \mathrm{diag}\{A_1, A_2, \dots, A_n\}$. Note that in Equation (8), without loss of generality, the number of basis functions is taken to be even. For the particular case of the Fourier basis, where

$$\Phi(t) = \Big[\cos(\omega_0 t) \quad \sin(\omega_0 t) \quad \cos(2\omega_0 t) \quad \sin(2\omega_0 t) \quad \dots \quad \cos\left(\frac{N}{2}\omega_0 t\right) \quad \sin\left(\frac{N}{2}\omega_0 t\right)\Big], \tag{9}$$

then,

$$\mathcal{R}_k^o = \mathbb{R}\mathrm{e}\{g_o(\jmath\omega_k)\}, \quad \mathcal{I}_k^o = \mathbb{I}\mathrm{m}\{g_o(\jmath\omega_k)\},$$

where $g_o(\jmath\omega_k)$ represents the nominal frequency response of the system at frequencies ω_k, if the system is defined by a set of linear differential equations, and $\mathbb{R}\mathrm{e}\{\cdot\}$ and $\mathbb{I}\mathrm{m}\{\cdot\}$ are the *real-part* and *imaginary-part* operators, respectively. It is important to note that, due to the 2×2 block diagonal nature of the representation, $\mathbf{G_o}$, defined in Equation (8), can be depicted in the plane $\mathcal{R}\times\mathcal{I}$.

Though not considered within this study, if the dynamics of the system under analysis constitute a nonlinear mapping, several techniques can be applied to obtain an approximate representation in terms of Equation (8). For an in-depth discussion about the approximation of nonlinear representations, the reader is referred to Bacelli, Genest, and Ringwood (2015).

2.3 Nominal optimal solution

By substituting Equation (7) into the approximate absorbed energy expression stated in Equation (6), the following equality is obtained:

$$J_N = -\frac{T}{2}\hat{\mathbf{u}}^\intercal \mathbf{G_o}(\hat{\mathbf{u}} + \hat{\mathbf{e}}), \tag{10}$$

which is a quadratic function of the variable $\hat{\mathbf{u}}$. In essence, in Equation (10), the state variables have been eliminated by substitution, and the optimisation is carried out over the control variable $\hat{\mathbf{u}}$ only. More importantly, the constrained optimisation problem, given by the objective function describing the total absorbed energy J_N and the linear equality constraints describing the system dynamics in Equation (7), has been transformed into an unconstrained quadratic program. Then, for the nominal model, if the concavity of Equation (10) can be guaranteed, the maximisation problem can be solved as a feasible quadratic programming problem. Thus, the concavity of J_N defines the feasibility condition. It is important to highlight that the concavity condition holds for WEC control, due to the passivity of the system (all terms in the diagonal of $\mathbf{G_o}$ are positive); thus, $(\mathbf{G_o} + \mathbf{G_o}^\intercal)^{-1}$ is a positive definite matrix, guaranteeing existence of a global maximum for Equation (10).

Therefore, the optimal formulation is stated as

$$\hat{\mathbf{u}}_o^\star \leftarrow \max_{\forall \hat{\mathbf{u}}_o \in \mathbb{R}^N} J_N, \tag{11}$$

where $\mathbf{u_o^\star}$, for the unconstrained quadratic problem, which maximises Equation (6), is then:

$$\hat{\mathbf{u}}_o^\star = -(\mathbf{G_o} + \mathbf{G_o}^\intercal)^{-1}\mathbf{G_o}\hat{\mathbf{e}},$$

The expression in Equation (11) will be used in the robust formulation in Section 3. Then, the optimal value of J_N, when Equation (11) is substituted in Equation (6), is:

$$J_N^\star = \frac{T}{2}\hat{\mathbf{u}}_o^{\star\intercal}\mathbf{G_o}(\hat{\mathbf{u}}_o^\star + \mathbf{e}).$$

3. Generic solution foundations

The basics of spectral and pseudospectral methods, for the nominal case, have been described in Section 2, showing the application procedure of these techniques. To proceed with the approach, it is necessary to have a precise description of the system either in terms of its analytical description, i.e. in a general sense as in Equation (1), or using the frequency response of the system defined in Equation (8), when the basis functions are defined as in Equation (9).

Nevertheless, in a more realistic situation, when the real system $\mathbf{G}$ does not match the nominal one, a representation of the real system can be obtained by the addition of a bounded disturbance $\Delta \in \mathbb{R}^{N\times N}$:

$$\mathbf{G} = \mathbf{G_o} + \Delta,$$

where Δ must be properly structured, depending on the selected basis functions, and takes the following form:

$$\Delta = \bigoplus_{k=1}^{N/2} \begin{bmatrix} \delta_k^{\mathcal{R}} & \delta_k^{\mathcal{I}} \\ -\delta_k^{\mathcal{I}} & \delta_k^{\mathcal{R}} \end{bmatrix},$$

which allows for the redefinition of the objective function:

$$J_N = -\frac{T}{2}\hat{\mathbf{u}}^\intercal \bigoplus_{k=1}^{N/2} \left(\begin{bmatrix} \mathcal{R}_k^o & \mathcal{I}_k^o \\ -\mathcal{I}_k^o & \mathcal{R}_k^o \end{bmatrix} + \begin{bmatrix} \delta_k^{\mathcal{R}} & \delta_k^{\mathcal{I}} \\ -\delta_k^{\mathcal{I}} & \delta_k^{\mathcal{R}} \end{bmatrix} \right) (\hat{\mathbf{u}} + \hat{\mathbf{e}}). \tag{12}$$

For the Fourier basis,

$$g(\jmath\omega_k) = g_o(\jmath\omega_k) + \delta_k \Leftrightarrow \delta_k = g(\jmath\omega_k) - g_o(\jmath\omega_k),$$

where $\delta_k \in \mathbb{C}$ represents the uncertainty level at the frequency ω_k with $\delta_k^{\mathcal{R}} = \mathbb{R}\mathrm{e}\{\delta_k\}$ and $\delta_k^{\mathcal{I}} = \mathbb{I}\mathrm{m}\{\delta_k\}$.

Without loss of generality, Figure 2(a) depicts the situation for $N = 2$ and $k \in \{1, 2, 3\}$. In Figure 2(a), the black points represent the nominal model, the diamonds show the real system location and the solid vectors (arrows) point to the nominal model coordinate locations. The absolute value of the vectors represents the magnitude of the system in the selected set of basis functions.

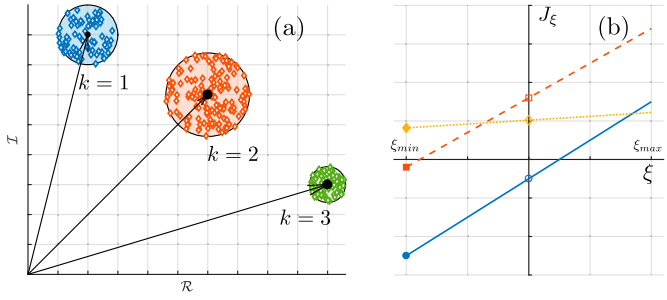

Figure 2. (a) The nominal model is represented by the solid black points. The diamonds show different possible locations for the real model **G** for $k = 1,2$ and 3. (b) Best-WCP sketch when $N = 1$. The uncertainty is represented with the variable $\xi \in [\xi_{\min}, \xi_{\max}]$, while the objective function is illustrated with the variable J_ξ. $\xi = 0$ represents the nominal case. The dashed orange line represents the objective function value when $\hat{\mathbf{u}}_o^\star$ is applied to the objective function while ξ varies. The solid blue line represents the use of a generic input $\hat{\mathbf{u}}$. The dotted yellow line represents the effect of using a robust input $\hat{\mathbf{u}}_r^\star$ in terms of the Best-WCP.

3.1 Best-worst case performance

This study seeks an approach which restates the problem defined in Equation (11) into a *Non-Probabilistic Robust Optimisation Problem*.

A sketch of the basic guidelines behind the formulation is depicted in Figure 2(b) for $N = 1$. The uncertainty set is represented by the variable $\xi \in [\xi_{\min}, \xi_{\max}]$, while the objective function is illustrated by the variable J_ξ. The intersection of each line (solid, dashed and dotted) with the $\xi = 0$ axis indicates the value of the objective function for the nominal case (empty markers) while, on the left-hand side, $\xi = \xi_{\min}$, the WCP for each signal is reached (filled markers). The dashed orange line represents the objective function value when the *nominal (non-robust) optimal input* $\hat{\mathbf{u}}_o^\star$ is applied to the objective function. The solid blue line represents the case when a generic input $\hat{\mathbf{u}}$ is applied. Finally, the dotted yellow line represents the effect of the use of a robust input $\hat{\mathbf{u}}_r^\star$ in terms of the Best-WCP, reaching the optimal WCP value over all the possible values of ξ. $\hat{\mathbf{u}}_r^\star$ minimises the losses in the cost function due to deviations from the nominal case due to the uncertainty term. Figure 2(b) shows how the use of a robust input, in terms of the Best-WCP, gives better performance over the complete variation set. For the nominal case, the dashed line reaches the optimal value (maximum) for the objective function J_ξ. However, the use of $\hat{\mathbf{u}}_o^\star$ can result in a significant performance deterioration, even making the captured power negative for some subset of ξ. For the case of power production, negative values in the objective function means taking energy from the grid instead of providing it. When $\hat{\mathbf{u}}_r^\star$ is used, there is a loss of performance in the nominal case, although the overall performance is more even over the uncertainty set.

Using the feasibility condition for the nominal case defined in Section 2.3, the robust control statement can be defined as shown below:

$$\hat{\mathbf{u}}_r^\star \leftarrow \max_{\hat{\mathbf{u}} \in \mathbb{R}^N} \min_{\Delta \in \mathcal{U}} J_N, \tag{13}$$

where $\mathcal{U}$ represents the set of all possible uncertainties. The last definition is a robust quadratic formulation and, more generally, can be rewritten into a minimax problem (Verdu & Poor, 1984). Furthermore, the uncertainty set must be defined properly in order to preserve the concavity and feasibility of the problem. Some comments about the definition of this set will be made in Section 3.2. On the other hand, as is usual in optimisation problems, the formulation is open to the systematic inclusion of constraints (equalities, inequalities, nonlinear constraints, etc).

Generally, the solution of robust optimisation problems involves creating a deterministic equivalent problem called the robust counterpart. This can be seen in Ben-Tal and Nemirovski (1998) and Ben-Tal, Nemirovski, and Roos (2002). Nevertheless, due to nonlinearities, if constraints are included in the formulation, this approach does not have a robust counterpart such as those mentioned in the bibliography. In addition, no specific structure for the uncertainty set has been adopted; however, even if the uncertainty has a specific structure, the introduced approach would still remain beyond the set of quadratic robust problems typical of the literature (Gorissen, Yanıkoğlu, & den Hertog, 2015; Marandi, Ben-Tal, den Hertog, & Melenberg, 2017).

Within this framework, in Sections 3.2–3.4, the optimal problem is tackled in order to find a general solution in two different ways. When the uncertainty is structured via circular and polytopic geometries, an analytical methodology is proposed. Subsequently, a (suboptimal) numerical procedure, which can be applied to any case, even to non-structured uncertainties, is shown. A further advantage of the numerical approach is that it can be easily extended to constrained cases, for example, bounding the space of possible solution vectors $\hat{\mathbf{u}}$.

3.2 Generic solution foundations

Here, the problem stated in Equation (13) is solved using two different methodologies: one analytical and one numerical. For the analytical case, circular and polytopic uncertainty structures are addressed. In a discrete sense, by the use of a grid over the uncertainty set, for general uncertainty structures, a numerical but suboptimal solution approach is proposed. Although suboptimal, the solution of the numerical approach can be arbitrarily improved by an iterative refining process. In addition, this approach allows for the inclusion of constraints to the control formulation.

3.2.1 General comments

The general objective function, stated as in Equation (12), can be rewritten as follows:

$$J_N = -\frac{T}{2}\left(\hat{\mathbf{u}}^\intercal \bigoplus_{k=1}^{N/2} \begin{bmatrix} e_k + u_k & e_{2k} + u_{2k} \\ e_{2k} + u_{2k} & -(e_k + u_k) \end{bmatrix} \bar{\delta} + f(\hat{\mathbf{e}}, \hat{\mathbf{u}})\right), \tag{14}$$

with $\bar{\delta} = [\delta_1^{\mathcal{R}}\ \delta_1^{\mathcal{I}}\ \dots\ \delta_{N/2}^{\mathcal{R}}\ \delta_{N/2}^{\mathcal{I}}]$ and

$$f(\hat{\mathbf{e}}, \hat{\mathbf{u}}) = \sum_{k=1}^{N/2} (e_{2k} + u_{2k})(\mathcal{I}_k^o u_{2k-1} + \mathcal{R}_k^o u_{2k}) - (e_{2k-1} + u_{2k-1})(\mathcal{I}_k^o u_{2k} - \mathcal{R}_k^o u_{2k-1}),$$

which shows that J_N is affine in $\bar{\delta}$. Then, the solution of the optimal formulation is reached on the convex hull of the uncertainty

set. Furthermore, when the uncertainty is structured as a convex polytope, if the optimal solution exists, it will be at one of the vertices of the polytope (Boyd & Vandenberghe, 2004).

Figure 3(a,b) show two different examples of boundary schemes used in this study, a convex polytope (specifically a square) and a circle, respectively. The set of all possible locations of the real system is given by $\mathcal{P}_k$, where the points on and within the hull of the geometry are included. In particular, $(\mathcal{R}_k, \mathcal{I}_k)$ represents the location of the real system within the geometry, while $(\mathcal{R}_k^o, \mathcal{I}_k^o)$ is the location of the nominal system, as illustrated in Figure 3(a,b).

In the case of the convex polytope, as shown in Figure 3(a), the geometry is defined by the set of vertices $\{\hat{\delta}_k^1\ \hat{\delta}_k^2\ \dots\ \hat{\delta}_k^{p_k}\}$, where p_k defines the number of vertices of the polytope used in case k. Hence, each $\hat{\delta}_k^j = (\hat{\delta}_k^{\mathcal{R}^j}, \hat{\delta}_k^{\mathcal{I}^j})$ is defined such that the bounds of the real system at the vertices are $\bar{\mathcal{R}}_k^j = \mathcal{R}_k^o + \hat{\delta}_k^{\mathcal{R}^j}$ and $\bar{\mathcal{I}}_k^j = \mathcal{I}_k^o + \hat{\delta}_k^{\mathcal{I}^j}$, with $j = 1, \dots, p_k$.

The circular case, depicted in Figure 3(b), can be defined in terms of a radius $0 \le \rho_k \le \bar{\rho}_k$ and an angle $0 \le \theta_k < 2\pi$, thus

$$\delta_k^{\mathcal{R}} = \mathbb{R}\mathrm{e}\{\rho_k\, \mathrm{e}^{\jmath\theta_k}\}, \quad \delta_k^{\mathcal{I}} = \mathbb{I}\mathrm{m}\{\rho_k\, \mathrm{e}^{\jmath\theta_k}\},$$

which must be repeated for each k-block in Equation (12). Then, for both cases (polytope and circle),

$$\mathcal{R}_k = \mathcal{R}_k^o + \delta_k^{\mathcal{R}}, \quad \mathcal{I}_k = \mathcal{I}_k^o + \delta_k^{\mathcal{I}},$$

where $(\delta_k^{\mathcal{R}}, \delta_k^{\mathcal{I}})$ represents the deviation from the nominal model and $(\mathcal{R}_k, \mathcal{I}_k) \in \mathcal{P}_k$. On the other hand, Equation (12) can be expressed as:

$$J_N = -\frac{T}{2}\sum_{k=1}^{N/2} \mathcal{R}_k(u_{2k-1}^2 + u_{2k}^2) + u_{2k}(e_{2k}\mathcal{R}_k - e_{2k-1}\mathcal{I}_k) + u_{2k-1}(e_{2k}\mathcal{I}_k - e_{2k-1}\mathcal{R}_k). \tag{15}$$

The expression in Equation (15) shows that the problem concavity will be consistent (for both nominal and real system) with the sign of each $\mathcal{R}_k$. Thus,

$$\mathcal{R}_k = \mathcal{R}_k^o + \delta_k^{\mathcal{R}} > 0. \tag{16}$$

Equation (16) explicitly shows the feasibility condition mentioned in Section 2.3, for both the nominal ($\delta_k^{\mathcal{R}} = 0$) and robust ($\delta_k^{\mathcal{R}} \neq 0$) cases. If $\mathcal{R}_k > 0$, then concavity is guaranteed, and thus the maximisation problem stated in Equation (10), as a quadratic programming problem, has a feasible formulation and an optimal solution.

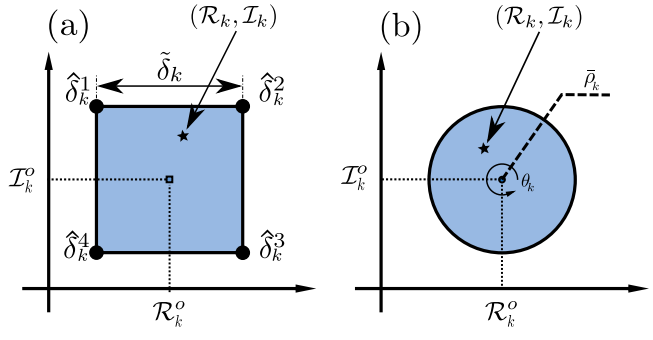

Figure 3. Two different boundaries for the uncertainty set. The real value $(\mathcal{R}_k, \mathcal{I}_k)$ ($\star$), is inside the boundary. The nominal value is, in (a) and (b), at $(\mathcal{R}_k^o, \mathcal{I}_k^o)$. (a) Convex polytopic set. (b) Convex and circular set.

Finally, if the optimal solution can be expressed as:

$$\hat{\mathbf{u}}^\star = \bigoplus_{k=1}^{N/2} -\frac{1}{2}\begin{bmatrix} 1 & \frac{\mathcal{I}_k}{\mathcal{R}_k} \\ -\frac{\mathcal{I}_k}{\mathcal{R}_k} & 1 \end{bmatrix} \hat{\mathbf{e}} \Leftrightarrow \left.\frac{\partial J_N}{\partial \hat{\mathbf{u}}}\right|_{\hat{\mathbf{u}}=\hat{\mathbf{u}}^\star} = 0 \tag{17}$$

then, by substituting $\hat{\mathbf{u}}^\star$ from Equation (17) into Equation (12),

$$J_N^\star = \frac{T}{8}\sum_{k=1}^{N/2} \frac{(\mathcal{R}_k^2 + \mathcal{I}_k^2)(e_{2k-1}^2 + e_{2k}^2)}{\mathcal{R}_k}. \tag{18}$$

In Sections 3.3 and 3.4, two solution methodologies for the Best-WCP are developed. The first, in Section 3.3, based on an analytic approach (which given some insight into the workings), is limited to circular and polytopic convex boundaries, and cannot consider system physical constraints. In Section 3.4, the scope of the problem is extended in the numerical formulation to consider uncertainty sets of arbitrary shape, adding the ability to consider physical system constraints.

3.3 Analytical solution approach

3.3.1 Circular boundary

Due to the fact that the worst case solution will be reached on the hull of the circle ($\rho_k = \bar{\rho}_k$), as shown in Equation (14), $\mathcal{R}_k$ and $\mathcal{I}_k$ can be replaced by:

$$\mathcal{R}_k = \mathcal{R}_k^o + \delta_k^{\mathcal{R}} = \mathcal{R}_k^o + \bar{\rho}_k \cos\theta_k$$
$$\mathcal{I}_k = \mathcal{I}_k^o + \delta_k^{\mathcal{I}} = \mathcal{I}_k^o + \bar{\rho}_k \sin\theta_k$$

Replacing these definitions in Equation (18), get:

$$J_N^\star(\theta_1, \dots, \theta_{\frac{N}{2}}) = \frac{T}{8}\sum_{k=1}^{N/2} \frac{\begin{array}{c}[\mathcal{R}_k^{o2} + \mathcal{I}_k^{o2} + 2\bar{\rho}_k(\mathcal{R}_k^o \cos\theta_k + \mathcal{I}_k^o \sin\theta_k) \\ +\bar{\rho}_k^2](e_{2k-1}^2 + e_{2k}^2)\end{array}}{\mathcal{R}_k^o + \bar{\rho}_k \cos\theta_k}, \tag{19}$$

and

$$\hat{\mathbf{u}}_r^\star = \bigoplus_{j=1}^{N/2} -\frac{1}{2}\begin{bmatrix} 1 & \mathcal{B}_k^\star \\ -\mathcal{B}_k^\star & 1 \end{bmatrix}, \quad \text{where } \mathcal{B}_k^\star = \frac{\mathcal{I}_k^o + \bar{\rho}_k \sin\theta_k^\star}{\mathcal{R}_k^o + \bar{\rho}_k \cos\theta_k^\star}. \tag{20}$$

To obtain the Best-WCP, the minimum value of the expression in Equation (19) is studied:

$$\frac{\partial J_N^\star}{\partial \theta_k} = \frac{T}{8}\frac{\begin{array}{c}\bar{\rho}_k[(\bar{\rho}_k^2 + \mathcal{I}_k^{o2} - \mathcal{R}_k^{o2})\sin\theta_k \\ +2\mathcal{R}_k^o\mathcal{I}_k^o\cos\theta_k + 2\bar{\rho}_k\mathcal{I}_k^o]\end{array}}{(\mathcal{R}_k + \bar{\rho}_k\cos\theta_k)^2}.$$

Thus,

$$\left.\frac{\partial J_N^\star}{\partial \theta_k}\right|_{\theta_k=\theta_k^\star} = 0 \Rightarrow \frac{\partial J_N^\star}{\partial \theta_k} = 0 \Leftrightarrow (\bar{\rho}_k^2 + \mathcal{I}_k^{o2} - \mathcal{R}_k^{o2})\sin\theta_k^\star + 2\mathcal{R}_k^o\mathcal{I}_k^o\cos\theta_k^\star + 2\bar{\rho}_k\mathcal{I}_k^o = 0$$

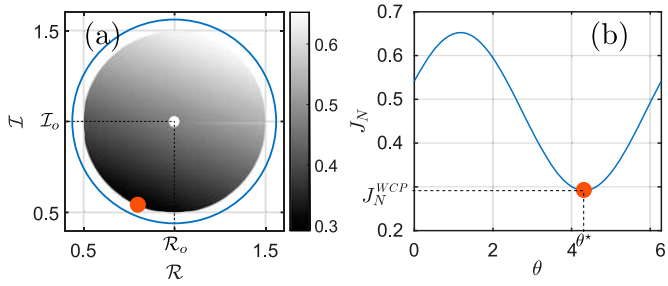

Figure 4. Example of the robust procedure application, for the circular case, when $N=2$, $\mathcal{R}_k^o = \mathcal{I}_k^o = 1$, $\hat{\mathbf{e}} = [\frac{\sqrt{(2)}}{2} \ \frac{\sqrt{(2)}}{2}]^\intercal$, and $\bar{\rho} = 0.5$. (a) Performance J_N over the complete variation set. (b) J_N is depicted over the hull ($\rho = \bar{\rho}$), illustrated in (a) with the blue solid line. In both cases, (a) and (b), when $\theta = \theta^\star = 4.32$ and $J_N(\theta^\star) = 0.29$, the WCP is highlighted with a solid dot.

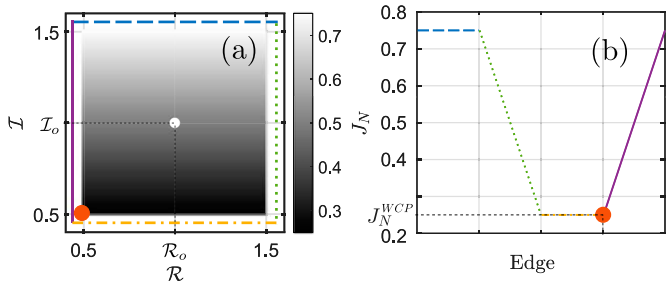

Figure 5. Example of the robust procedure application, for the polytopic case, when $N=2$, $\mathcal{R}_k^o = \mathcal{I}_k^o = 1$, and $\hat{\mathbf{e}} = [\frac{\sqrt{(2)}}{2} \ \frac{\sqrt{(2)}}{2}]^\intercal$. (a) Performance J_N over the complete variation set. (b) J_N is depicted over the hull, where the segments, illustrated with different line styles and colours, are indicated in (a). In both cases, (a) and (b), the WCP is highlighted with a solid dot.

$$\theta_k^\star = \frac{c_k^3}{\sqrt{{c_k^1}^2 + {c_k^2}^2}} - \arctan\frac{c_k^1}{c_k^2}, \tag{21}$$

with

$$c_k^1 = 2\mathcal{I}_k^o\mathcal{R}_k^o, \quad c_k^2 = \bar{\rho}_k^2 + \mathcal{I}_k^o - \mathcal{R}_k^{o2}, \quad c_k^3 = -2\bar{\rho}_k\mathcal{I}_k^o,$$

which gives the location for θ_k where J_N reaches the minimum over $\mathcal{U}$.

Replacing Equation (21) in (20), the input $\hat{\mathbf{u}}_r^\star$ that guarantees the Best-WCP is obtained. Finally, the Best-WCP is given by:

$$J_N^{\text{WCP}} = J_N^\star(\theta_1^\star, \ldots, \theta_{N/2}^\star)$$

Figure 4 shows an example of the robust procedure application, for the circular case, when $N=2$, $\mathcal{R}_k^o = \mathcal{I}_k^o = 1$, $\hat{\mathbf{e}} = [\frac{\sqrt{(2)}}{2} \ \frac{\sqrt{(2)}}{2}]^\intercal$ ($\|\hat{\mathbf{e}}\|_2 = 1$), and $\bar{\rho} = 0.5$. In Figure 4(a), the performance J_N, over the complete variation set, is shown. In Figure 4(b), J_N is depicted over the hull ($\rho = \bar{\rho}$). In both cases, when $\theta = \theta^\star = 4.32$ and $J_N(\theta^\star) = 0.29$, the WCP is highlighted with a solid dot. Finally, $\hat{\mathbf{u}}_r^\star = [-0.5893 \ -0.1179]^\intercal$.

3.3.2 Polytopic boundary

For the polytopic boundary, if the optimal solution exists, it will be on a vertex of the polytope. Then, for each $\mathcal{P}_k$ defined in Section 3.2.1, using Equation (18)

$$(\mathcal{R}_k^{j^\star}, \mathcal{I}_k^{j^\star}) \leftarrow j_k^\star \leftarrow \underset{j_k=1,\ldots,p_k}{\arg\min} J_N^\star\Big|_{\mathcal{R}_k=\bar{\mathcal{R}}_k^j,\, \mathcal{I}_k=\bar{\mathcal{I}}_k^j},$$

for $j_k = 1, \ldots, p_k$ and $k \in \{1, \ldots, N/2\}$. Defining the vertex for each k where the Best-WCP is reached, Equation (17) is used for the computation of $\hat{\mathbf{u}}_r^\star$. Then,

$$J_N^{\text{WCP}} = J_N^\star(\mathcal{R}_k^{j^\star}, \mathcal{I}_k^{j^\star}, \ldots, \mathcal{R}_{N/2}^{j^\star}, \mathcal{I}_{N/2}^{j^\star}).$$

Figure 5 shows an example of the robust procedure application, for the polytopic case, when $N=2$, $\mathcal{R}_k^o = \mathcal{I}_k^o = 1$, and $\hat{\mathbf{e}} = [\frac{\sqrt{(2)}}{2} \ \frac{\sqrt{(2)}}{2}]^\intercal$ ($\|\hat{\mathbf{e}}\|_2 = 1$). In Figure 5(a), the performance J_N, over the complete variation set, is shown. In Figure 5(b), J_N is depicted over the hull ($\rho = \bar{\rho}$). In both cases, when $\theta = \theta^\star = 4.32$ and $J_N(\theta^\star) = 0.29$, the WCP is highlighted with a solid dot. Finally, $\hat{\mathbf{u}}_r^\star = [-0.7071 \ 0]^\intercal$.

3.4 Numerical approach and custom bounding

In order to pose the problem in a standard form, Equation (13) is rewritten into a minimax framework:

$$\hat{\mathbf{u}}_r^\star \leftarrow \max_{\hat{\mathbf{u}}\in\mathbb{R}^N} \min_{\Delta\in\mathcal{U}} J_N = \min_{\hat{\mathbf{u}}\in\mathbb{R}^N} \max_{\Delta\in\mathcal{U}} -J_N.$$

To proceed with the numerical approach for the solution, the uncertainty space is discretised. Figure 6 shows different possible uncertainty sets and their discretisation in the plane $\mathcal{R} - \mathcal{I}$. From the discussion in Section 3.2.1 and Equation (14), some comments can be made for Figure 6(a–d):

(a) Non-polytopic convex set. Since the solution will be reached on the hull, then, the discretisation is focussed on the external points of the set. As the mesh is refined, the solution approaches the optimal value.
(b) Polytopic convex set. The solution will be on the vertices that define the set. Only the vertices should be taken into account in the discretisation. The solution will be exact (optimal).
(c) Non-convex polytopic set. In general, for non-convex structures (polytopic or non-polytopic) the optimal solution will be reached on the convex hull. For non-convex polytopes, the convex vertices should be only considered and, in this case, the solution will be exact (optimal).
(d) Arbitrary points set. The problem can be solved for an arbitrary set of points. The solution will be optimal over the set points.

Once the discretisation is carried out, then the problem is restated in terms of the discretised grid:

$$\min_{\hat{\mathbf{u}}\in\mathbb{R}^N} \max_{\Delta_i\in\mathcal{U}} \frac{T}{2}\hat{\mathbf{u}}^\intercal\mathbf{G}_i(\hat{\mathbf{u}} + \hat{\mathbf{e}}),$$

with $\mathbf{G}_i = \mathbf{G_o} + \Delta_i$, where Δ_i is the perturbation associated at each i-point selected for the grid.

In Figure 6(a–d), the small empty circles define a general grid, the large empty circles are points on the hull, and the solid green points should be in the discretisation. Following these specifications, the problem can be properly formulated in the

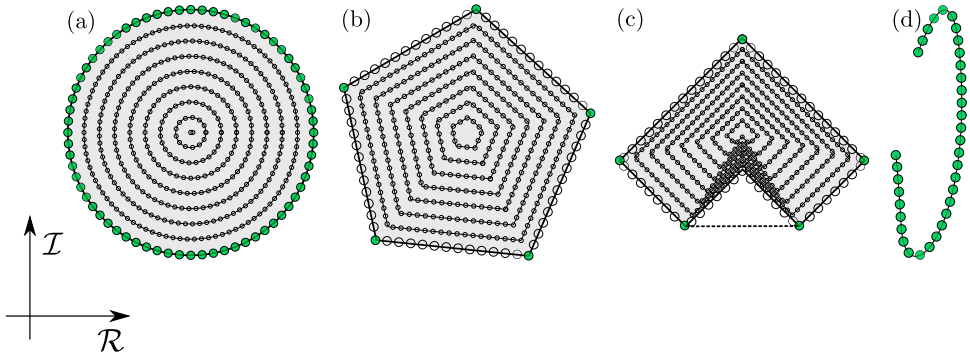

Figure 6. Different possible uncertainty sets and their meshing in the plane $\mathcal{R} - \mathcal{I}$. (a) Non-polytopic convex set. (b) Polytopic convex set. (c) Non-convex polytopic set. (d) Arbitrary points set. In (a)–(d), the small empty circles define a general grid, the large empty circles are points on the hull, and the solid green points are those that should be in the discretisation.

standard minimax form:

$$\begin{aligned} \min_{\hat{\mathbf{u}} \in \mathbb{R}^N} \max_{i} \quad & F_i(\hat{\mathbf{u}}) \\ \text{subject to} \quad & \mathcal{C}(\hat{\mathbf{u}}), \end{aligned} \tag{22}$$

where $F_i(\hat{\mathbf{u}}) = (T/2)\hat{\mathbf{u}}^\intercal \mathbf{G}_i(\hat{\mathbf{u}} + \hat{\mathbf{e}})$, and $\mathcal{C}(\hat{\mathbf{u}})$ is a set of constraints. When numerical solvers are used to compute the optimal solution of the problem stated in Equation (22), constraints can be straightforwardly included in the formulation. However, the analytical approach *for the constrained case* is beyond the scope of this study.

3.5 Practical aspects

Some practical aspects need to be highlighted:

Spectrum Definition. The method gives a procedure to compute the optimal input signal $\hat{\mathbf{u}}_r^\star$ ($u_r^\star(t)$), but also provides an uncertainty-based criterion on how to select the spectral components. When the spectral components are defined as in Section 3, in order to guarantee a feasible optimisation problem, the feasibility condition stated in Equation (16) must hold. Thus, spectral components that do not meet the feasibility condition must be removed from the set of basis functions.

Extreme Best-WCP. When the feasibility condition stated in Equation (16) is close to being violated, in other words, i.e. a high uncertainty level is present, the proposed method guarantees a minimum zero WCP. Using an approach exclusively based on the *nominal model*, there are no guarantees about the WCP, with the added risk of generating negative energy. Under the robust formulation, in order to avoid negative energy levels in extreme cases, the input signal is set to zero.

Discretisation Dependence on Uncertainty Level. When the problem is addressed using the numerical approach and the uncertainty set is non-polytopic, the mesh refinement should increase with the uncertainty level.

Uncertainty Estimation. The uncertainty set can be estimated in experimental data, nonlinearities, or parametric uncertainty in the physical parameters of the system, or a combination of these uncertainty sources. For a further description of different uncertainty sources, the reader is referred to Giorgi, Davidson, and Ringwood (2016) and Giorgi, Davidson, Jakobsen, Kramer, and Ringwood (2018) for experimental data uncertainty sources; to Penalba, Mérigaud, Gilloteaux, and Ringwood (2017) and Bacelli, Coe, Patterson, and Wilson (2017) for nonlinear uncertainty sources; and to Davidson, Giorgi, and Ringwood (2015) for physical parametric uncertainty sources. In addition, an important uncertainty source is related to excitation force estimation and forecasting. This uncertainty source is not considered in this study, since the inclusion of $F_e(t)$ estimation/forecasting errors leads to a different optimisation scenario, but will be the subject of a future study.

4. Application example

This section shows an application example of the robust framework introduced in Section 3. Considering that the proposed approach is based on a feedforward (FF) controller structure, a spectral *non-robust* FF controller (Bacelli & Ringwood, 2015) is used as a benchmark to allow a comparison with the results obtained with the presented robust FF controller. In the comparison, the robustness of each controller, in terms of the obtained worst-case performance, is assessed. Additionally, different uncertainty boundaries are used in this application example, showing the trade-off between conservativeness and system performance. To focus on the control problem, which is the main driver of this study, perfect knowledge of the wave excitation force is assumed.[2] Additionally, for the sake of clarity in the results, second order Fourier basis functions are used as projection space defined by Φ (see Section 2).

The application example is based on a spherical WEC model, as shown in Figure 7(a) (Falnes, 2002). The radius and mass of the device are 5 m and 33,543 kg, respectively. The system input and output are the total input force $u_i(t) = F_e(t) + u(t)$ and the device velocity $v(t)$, respectively, which are both defined with respect to the vertical axis. The block scheme is shown in Figure 7(b), where the controller block (which uses the excitation force $F_e(t)$ to compute the control signal $u(t)$ for maximising the absorbed energy), the free surface elevation $\eta(n)$, the family of models $g(\omega)$, and the mapping $g_e(\omega)$ from $\eta(t)$ to $F_e(t)$ are shown.

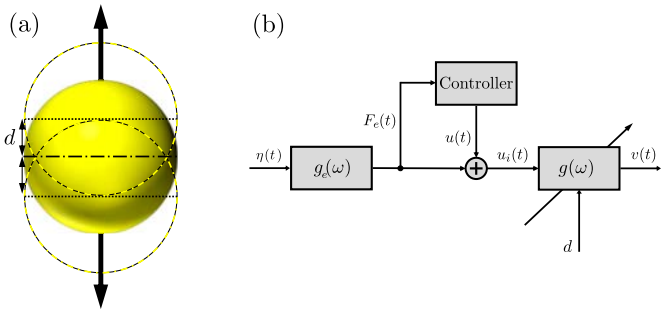

Figure 7. (a) Physical model of the spherical WEC. (b) System block scheme of the spherical WEC and controller, where the WEC total input force is $u_i(t) = F_e(t) + u(t)$, the WEC output considered is the device velocity $v(t)$, and $\eta(t)$ represents the free surface elevation. The controller block is shown, which uses the excitation force $F_e(t)$ to compute the control signal $u(t)$.

The data for the family of models $g(\omega)$, used in the application example, is generated using the boundary element method-based environment NEMOH (Babarit & Delhommeau, 2015; LHEEA, NEMOH-Presentation, 2017), obtaining the model frequency response at different operating points by varying the displacement $d \in [-1, 1]$, which represents the distance between the still water level and the center of the sphere (Figure 7(a)). For each d, a different frequency response is generated, obtaining a family of models for each particular frequency ω. Figure 8 shows the different frequency response, for each d, from the total input force $u_i(t) = F_e(t) + u(t)$ to the velocity $v(t)$. The excitation force $F_e(t)$ is determined from the free surface elevation $\eta(t)$, which is based on a JONSWAP spectrum (Hasselmann et al., 1973), $J_\eta(\omega)$, and $g_e(\omega)$, where $g_e(\omega)$ is obtained from NEMOH, as shown in Figure 7(b). The sea state parameters used in this study for $J_\eta(\omega)$ are a peak period $T_p = 8$ s, significant wave height $H_s = 2.5$ m, and a steepness parameter $\gamma = 3.3$. In Figure 9, the dashed blue line illustrates $|F_e(\omega)| = |g_e(\omega)||J_\eta(\omega)|$ and the solid orange line represents the normalised magnitude:

$$|\bar{g}_o(\omega)| = \frac{|g_o(\omega)|}{\max\{|g_o(\omega)|\}} \max\{|F_e(\omega)|\}, \tag{23}$$

where $g_o(\omega)$ indicates the frequency response for the device when $d = 0$ m and the operator $\max\{\cdot\}$ returns the maximum value of the function over the domain, in this case, ω. The normalisation $\bar{g}_o(\omega)$, expressed in Equation (23), is used to show how the system resonance frequency impacts on the resulting performance. The dotted red line, in Figure 9, shows the relationship $|F_e(\omega)\bar{g}_o(\omega)|$, which articulates the complete normalised model from wave ($\eta(t)$) to device motion ($v(t)$). The normalised magnitude, illustrated with the dotted red line in Figure 9, shows the most sensitive points in terms of the resulting performance at $\omega \approx 0.8$ rad/s, due to the $F_e(t)$ spectral distribution, and $\omega \approx 1.85$ rad/s, due to system resonance frequency.

This illustrative study is made assuming $N = 2$ ($\hat{\mathbf{u}}_o^\star$, $\hat{\mathbf{u}}_r^\star$, $\hat{\mathbf{e}} \in \mathbb{R}^2$ and $\mathbf{G}$, $\mathbf{G}_o \in \mathbb{R}^{2\times 2}$) and using the Fourier basis functions:

$$\Phi(t) = [\cos(\omega t) \quad \sin(\omega t)]$$

Given that, for this example, the excitation force is parametrised with two basis functions, i.e. a monochromatic approximation, and in order to get non-null projections over each basis function, for illustrative proposes, $\pi/4$ rad/s was used as initial phase for the representation of $F_e(t)$. Different selections for the initial phase will impact on the coordinate locations (coefficients of the approximation) of the control signal, but not on the absorbed energy. Each robust ($\hat{\mathbf{u}}_r^\star$) and the nominal input ($\hat{\mathbf{u}}_o^\star$) is computed for each frequency individually within the range $\omega \in [0, 10]$ rad/s, with the most significant results at $[0.4, 2]$ rad/s.

4.1 Illustrative results

In this section, the results obtained with the proposed (robust) approach are compared with those obtained with an equivalent non-robust approach (Bacelli & Ringwood, 2015). Note that both approaches are based on feedforward control structures.

Figure 10 shows the results for the robust controller and the comparison with the nominal approach, when the uncertainty set is defined by variations in d. For the case $\omega^\star = 2$ rad/s, Figure 10(a) shows the uncertainty set, depicted by the violet

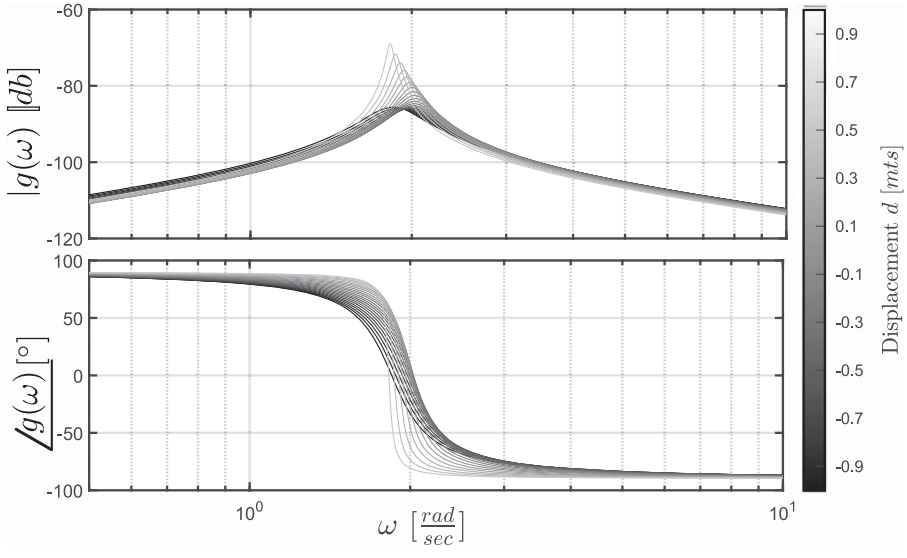

Figure 8. Frequency response for $g(j\omega)$ by varying the difference $d \in [-1, 1]$.

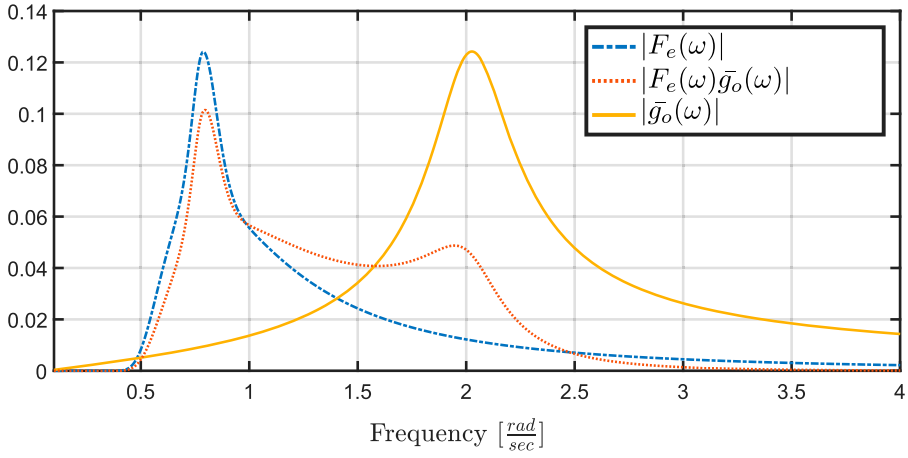

Figure 9. The magnitude $|F_e(\omega)|$ is represented with the dashed blue line. The normalised magnitude $\bar{g}_o(\omega)$ is depicted with the solid yellow line. The dotted red line represents the magnitude $|F_e(\omega)\bar{g}_o(\omega)|$.

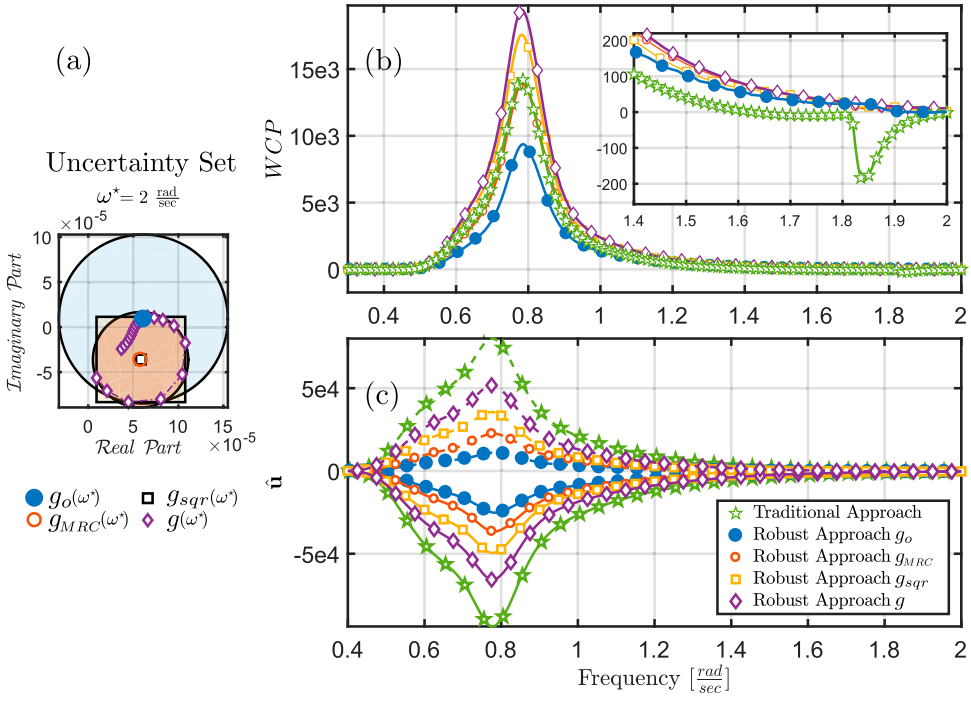

Figure 10. (a) Uncertainty set and different boundaries. (b) The WCP using the different inputs $\hat{\mathbf{u}}_r^\star$ and $\hat{\mathbf{u}}_o^\star$, with a close-up at $\omega \in [1.4,\ 2.0]$ rad/s. (c) Coordinates location of $\hat{\mathbf{u}}_r^\star$ and $\hat{\mathbf{u}}_o^\star$, where the solid and dashed lines represent the first and the second coordinate of the inputs ($\hat{\mathbf{u}}_o^\star$ and $\hat{\mathbf{u}}_r^\star$), respectively. The legend in (c) also applies for (b) and (c).

diamonds, used as an arbitrary point set ($g(\omega^\star)$) for the numerical approach, and three different uncertainty boundaries for the analytical solution: (1) a large circular boundary, represented by the blue circle, (2) a smaller circular boundary, illustrated by the orange circle, and (3) a square polytope, depicted by the yellow square. In addition, in Figure 10(a),

(1) the blue dot marker represents the location of the model when $d = 0$ ($g_o(\omega^\star)$), which is also the centre of the large circular boundary used in the comparison;
(2) the orange circular marker represents the centre of the minimum radius circle ($g_{\mathrm{MRC}}(\omega^\star)$) which contains all the violet diamonds, which is the smaller circular boundary used in the comparison;
(3) the black square marker represents the centre of the square polytope ($g_{\mathrm{sqr}}(\omega^\star)$); and
(4) the violet diamonds represents the real location for each d value ($g(\omega^\star)$);

Figure 10(b) shows the WCP obtained when each input $\hat{\mathbf{u}}_r^\star$ and $\hat{\mathbf{u}}_o^\star$, computed for each respective boundary, applied to the complete set of models using, for the computation of the nominal input $\hat{\mathbf{u}}_o^\star$, the set defined by $g_o(\omega)$. In Figure 10(b), the WCP is plotted using:

(1) the green line with empty star markers for the WCP, obtained when $\hat{\mathbf{u}}_o^\star$ is applied to the complete variation set (analytical solution);

(2) the blue line with dot markers, when $\hat{\mathbf{u}}_r^\star$ is computed using the large circular boundary (analytical solution) and applied to the complete variation set;
(3) the orange line with circular markers, when $\hat{\mathbf{u}}_r^\star$ is computed using the small circular boundary (analytical solution) and applied to the complete variation set;
(4) the yellow line with square markers, when $\hat{\mathbf{u}}_r^\star$ is computed using the square polytope boundary (analytical solution) and applied to the complete variation set; and
(5) the violet line with diamond markers, when $\hat{\mathbf{u}}_r^\star$ is computed using the set of arbitrary points defined with diamonds in Figure 10(a) (numerical solution) and applied to the complete variation set.

Using the same marker code as in Figure 10(b,c) shows the coordinate location for $\hat{\mathbf{u}}_o^\star$, and the different robust inputs $\hat{\mathbf{u}}_r^\star$.

4.2 Results analysis

Comparing the results of the two circular cases in Figure 10(b), the impact of the size of the boundaries, i.e. the conservativeness of the boundary, on the resulting performance, is highlighted. The larger the boundary is, the more conservative the approach, and the lower the consequent performance, as might be expected. Additionally, the violet line with diamond markers in Figure 10(b), when the robust approach is applied when considering the precise set of point which defines the uncertainty set, shows how the performance is improved by selecting non-conservative (or less conservative) boundaries.

On the other hand, Figure 10(b) shows that the robust approach never results in the *consumption* of power. However, the nominal controller results in negative energy, as shown in Figure 10(b), around $\omega = 1.85$ rad/s.

Finally, Figure 10(b) shows the most sensitive points, at $\omega \approx 0.8$ rad/s and $\omega \approx 1.85$ rad/s, which can also be observed in Figure 9. The first point, at $\omega \approx 0.8$ rad/s, is related to the frequency band with the largest power density for the excitation force $F_e(\omega)$, depicted in Figure 9 with the blue line. The second point, at $\omega \approx 1.85$ rad/s, is related to the device resonance frequency, illustrated in Figure 9 with the solid yellow line.

5. Conclusion

This study proposes a novel framework for computing and solving spectral and pseudospectral energy-related optimal control formulations in a robust sense, in terms of the Best-WCP. The case of an absorbed energy objective function is considered, showing the concavity condition that allows for a robust formulation. An analytical and explicit approach is introduced for structured cases, while a numerical approach allows an extension of the uncertainty bound to any set, as well as the inclusion of constraints. Furthermore, a set of practical hints are provided to properly handle uncertainty boundaries. For the numerical approach, this study shows how to correctly select the mesh size, showing four general different cases: non-polytopic convex sets, polytopic convex sets, non-convex polytopic sets, and arbitrary point sets. Furthermore, when the solution is suboptimal, the procedure to improve the grid and bring the solution closer to the optimal is indicated.

The application example shows how the robust approach for the WEC case ensures that the resulting absorbed power will not be negative, guaranteeing positive generated energy. The conservativeness can be improved by a closer fitting of the uncertainty boundary. In this sense, this study shows how a correct uncertainty bound can significantly improve the results. Different bounds are considered in this study, including the one that exactly matches the true system, $g_o(\omega)$. For the bound based on $g_o(\omega)$, a circle containing the complete uncertainty set is introduced. With this, Section 4 shows how the adaptation of the bound can considerably improve the performance obtained, due to the reduction in conservativeness. Furthermore, due to the realistic spectral definition of $F_e(t)$, the application example exposes the sensitivity of the obtained performance to the excitation force spectrum of both the robust case, considering each different uncertainty boundary, and the non-robust case.

Finally, this study shows how the lack of uncertainty consideration in the problem statement can result in negative generated energy. The application of a nominal controller is compared with the robust approach, showing significant performance degradation for the nominal case against the robust approach. Moreover, the robust approach provides convergence guarantees to the Best-WCP, ensuring better performance for any model within the uncertainty bound.

Notes

1. The proposed framework is an intermediate step in a number of implementable feedforward control strategies such as, for example, strategies based on receding horizon control (Bacelli & Ringwood, 2015; Genest & Ringwood, 2017).
2. Note that this is a relatively standard assumption in the WEC control literature (Faedo et al., 2017).

Acknowledgements

Thanks to Eng. Nicolás Faedo for the continuous discussion during this study.

Disclosure statement

No potentsial conflict of interest was reported by the authors.

Funding

This material is based upon works supported by Science Foundation Ireland under [grant no. 13/IA/1886].

ORCID

Demián Garcia-Violini http://orcid.org/0000-0002-3131-7575
John V. Ringwood https://orcid.org/0000-0003-0395-7943

References

Babarit, A., & Delhommeau, G. (2015). Theoretical and numerical aspects of the open source BEM solver NEMOH. In *Proceedings of 11th European wave and tidal energy conference (EWTEC 2015)*, Nantes, France.
Bacelli, G. (2014). *Optimal control of wave energy converters* (Not unpublished) (Ph.D. dissertation). National University of Ireland, Maynooth, Ireland.
Bacelli, G., Coe, R. G., Patterson, D., & Wilson, D. (2017). System identification of a heaving point absorber: Design of experiment and device modeling. *Energies*, *10*(4), 472.

Bacelli, G., Genest, R., & Ringwood, J. V. (2015). Nonlinear control of flap-type wave energy converter with a non-ideal power take-off system. *Annual Reviews in Control*, *40*, 116–126.

Bacelli, G., & Ringwood, J. V. (2015). Numerical optimal control of wave energy converters. *IEEE Transactions on Sustainable Energy*, *6*(2), 294–302.

Bacelli, G., Ringwood, J. V., & Gilloteaux, J. C. (2011). A control system for a self-reacting point absorber wave energy converter subject to constraints. *IFAC Proceedings Volumes*, *44*(1), 11387–11392.

Ben-Tal, A., & Nemirovski, A. (1998). Robust convex optimization. *Mathematics of Operations Research*, *23*(4), 769–805.

Ben-Tal, A., Nemirovski, A., & Roos, C. (2002). Robust solutions of uncertain quadratic and conic-quadratic problems. *SIAM Journal on Numerical Analysis*, *13*(2), 535–560.

Boyd, J. P. (2001). *Chebyshev and fourier spectral methods* (2nd ed.). Mineola, New York: Dover Publications.

Boyd, S., & Vandenberghe, L. (2004). *Convex optimization*. Cambridge: Cambridge University Press.

Cummins, W. E. (1962). The impulse response function and ship motions. *Schiffstechnik*, *47*, 101–109.

Davidson, J., Genest, R., & Ringwood, J. V. (2018). Adaptive control of a wave energy converter. *IEEE Transactions on Sustainable Energy*, *9*(4), 1588–1595.

Davidson, J., Giorgi, S., & Ringwood, J. V. (2015). Linear parametric hydrodynamic models for ocean wave energy converters identified from numerical wave tank experiments. *Ocean Engineering*, *103*, 31–39.

Faedo, N., Olaya, S., & Ringwood, J. V. (2017). Optimal control, MPC and MPC-like algorithms for wave energy systems: An overview. *IFAC Journal of Systems and Control*, *1*, 37–56.

Fahroo, F., & Ross, I. M. (2008). Pseudospectral methods for infinite-horizon nonlinear optimal control problems. *Journal of Guidance, Control, and Dynamics*, *31*(4), 927–936.

Falnes, J. (2002). *Ocean waves and oscillating systems: Linear interactions including wave-energy extraction*. Cambridge: Cambridge University Press.

Finlayson, B. A., & Scriven, L. E. (1966). The method of weighted residuals: A review. *Applied Mechanics Reviews*, *19*(9), 735–748.

Fornberg, B. (1996). *A practical guide to pseudospectral methods*. Cambridge: Cambridge University Press.

Fusco, F., & Ringwood, J. V. (2014). Hierarchical robust control of oscillating wave energy converters with uncertain dynamics. *IEEE Transactions on Sustainable Energy*, *5*(3), 958–966.

Genest, R., & Ringwood, J. V. (2016). A critical comparison of model-predictive and pseudospectral control for wave energy devices. *Journal of Ocean Engineering and Marine Energy*, *2*(4), 485–499.

Genest, R., & Ringwood, J. V. (2017). Receding horizon pseudospectral control for energy maximization with application to wave energy devices. *IEEE Transactions on Control Systems Technology*, *25*(1), 29–38.

Giorgi, S., Davidson, J., Jakobsen, M., Kramer, M., & Ringwood, J. V. (2018). Identification of dynamic models for a wave energy converter from experimental data. *Ocean Engineering*. (Under Revision).

Giorgi, S., Davidson, J., & Ringwood, J. V. (2016). Identification of wave energy device models from numerical wave tank data-part 2: Data-based model determination. *IEEE Transactions on Sustainable Energy*, *7*(3), 1020–1027.

Gong, Q., Kang, W., & Ross, I. M. (2006). A pseudospectral method for the optimal control of constrained feedback linearizable systems. *IEEE Transactions on Automatic Control*, *51*(7), 1115–1129.

Gorissen, B. L., Yanıkoğlu, İ., & den Hertog, D. (2015). A practical guide to robust optimization. *Omega*, *53*, 124–137.

Hasselmann, K., Barnett, T. P., Bouws, E., Carlson, H., Cartwright, D. E., Enke, K., ... Walden, H. (1973). Measurements of wind wave growth and swell decay during the Joint North Sea Wave Project (JONSWAP). *Deutches Hydrographisches Institut*, *8*, 95.

Herber, D. R., & Allison, J. T. (2013). Wave energy extraction maximization in irregular ocean waves using pseudospectral methods. In *Proceedings of the ASME 2013 international design engineering technical conference and computers and information in engineering conference (DETC2013)* (Vol. 3), Portland, OR, USA.

LHEEA, NEMOH-Presentation (2017). Laboratoire de Recherche en Hydrodynamique Énergetique et Environnement Atmospherique. Retrieved from https://goo.gl/yX8nFu.

Li, G., & Belmont, M. R. (2014). Model predictive control of sea wave energy converters—Part II: The case of an array of devices. *Renewable Energy*, *68*, 540–549.

Liu, R., & Li, S. (2014). Optimal integral sliding mode control scheme based on pseudospectral method for robotic manipulators. *International Journal of Control*, *87*(6), 1131–1140.

Marandi, A., Ben-Tal, A., den Hertog, D., & Melenberg, B. (2017). Extending the scope of robust quadratic optimization. *Available on Optimization Online*. (Mathematical Optimization Society).

Nikooeinejad, Z., Delavarkhalafi, A., & Heydari, M. (2018). Application of shifted Jacobi pseudospectral method for solving (in)finite-horizon min-max optimal control problems with uncertainty. *International Journal of Control*, *91*(3), 725–739.

Penalba, M., Mérigaud, A., Gilloteaux, J. C., & Ringwood, J. V. (2017). Influence of nonlinear Froude–Krylov forces on the performance of two wave energy points absorbers. *Journal of Ocean Engineering and Marine Energy*, *3*(3), 209–220.

Richter, M., Magaña, M. E., Sawodny, O., & Brekken, T. K. (2014). Power optimisation of a point absorber wave energy converter by means of linear model predictive control. *IET Renewable Power Generation*, *8*(2), 203–215.

Ringwood, J. V., Bacelli, G., & Fusco, F. (2014). Energy-maximizing control of wave-energy converters: The development of control system technology to optimize their operation. *IEEE Control Systems*, *34*(5), 30–55.

Ross, I. M., & Karpenko, M. (2012). A review of pseudospectral optimal control: From theory to flight. *Annual Reviews in Control*, *36*(2), 182–197.

Verdu, S., & Poor, H. (1984). On minimax robustness: A general approach and applications. *IEEE Transactions on Information Theory*, *30*(2), 328–340.

Wahyudie, A., Jama, M. A., & Saed, O. (2015). Robust hierarchical control strategy for heaving wave energy converters. In *Proceedings of IEEE Oceans conference*, Genova.